Conversion of Methane to Ethylene with $BaCe_{0.9}Y_{0.1}Co_xO_{3-\delta}$ Hydrogen Permeation Membrane①

LIU Yun[a, b] YUAN Sheng-Ze[b, c] XIE Kui[b]②

[a] (*College of Chemistry, Fuzhou University, Fuzhou* 350116, *China*)

[b] (*Key Laboratory of Design and Assembly of Functional Nanostructures, Fujian Institute of Research on the Structure of Matter, Chinese Academy of Sciences, Fuzhou* 350002, *China*)

[c] (*College of Chemistry and Materials Science, Fujian Normal University, Fuzhou* 350007, *China*)

ABSTRACT Dehydrogenation coupling of methane (DCM), which can be effectively used to produce low carbon alkenes, has the advantages of rich raw materials, simple reaction device, low energy consumption, etc. Herein, we report a series of Co doped perovskite porous-dense $BaCe_{0.9}Y_{0.1}Co_xO_{3-\delta}$ (BCYC*x*) membrane for DCM. After treatment in a reduced atmosphere, a large number of Co nanoparticles will exsolute on the surface of BCY. The metal-oxide interface is helpful to activate the C–H bonds, inhibit the carbon deposition, and so on. The XRD, SEM and XPS prove that Co nanoparticles homogeneously distributed on the BCYC*x* porous layers, which will create a large quantity of catalytic active sites. At 1100 ℃, the highest concentration of C_2 product was 5.66% (5.25% ethane + 0.41% ethylene) in output gas when methane conversion reaches a maximum value of 24.8%, and the C_2 selectivity gets to 45.6%. We further demonstrate the catalytic performance of high-temperature DCM without obvious decrease after running for 30 hours.

Keywords: mixed-conducting, dehydrogenation, methane, metal nanoparticle, membrane;

DOI: 10.14102/j.cnki.0254–5861.2011–3055

1 INTRODUCTION

Low carbon alkenes, mainly obtained from naphtha cracking, are the most important parts of the petrochemical industry[1]. As the extremely important basic raw materials in chemical industry, low carbon olefins are being consumed more and more frequently, which made the traditional petrochemical route production of low carbon olefins far from meeting the market demand[2, 3]. Natural gas, mainly including CH_4, to syngas has been extensively studied because it can further react to form light olefins. The synthesis gas can be indirectly converted to low carbon olefins.The CuZnAl (CZA) was taken as catalyst to convert synthesis gas to the methanol intermediates and then the intermediates can be transformed to the olefin by the molecular sieve[4-8]. In addition, the synthesis gas can also be directly converted to olefins by Fischer-Tropsch reaction[9, 10]. However, direct and indirect syntheses have the problems of high energy cost and complex reaction process, respectively. The complexity of the reaction process and the variety of products make the utilization efficiency of carbon atoms relatively low.

Some methods, such as oxidation coupling of methane (OCM)[11] or dehydrogenation coupling of methane (DCM)[12], can be used to produce ethylene directly from methane. Compared with OCM, DCM does not introduce oxygen, which avoids the formation of carbon oxides. DCM has simple process and can efficiently use methane to synthesize high-value chemicals. This is crucial to the adjustment of chemical industry chain. In addition, it helps solve environmental problems in ways that reduce emissions at source. Of course, the direct conversion of CH_4 to C_2H_4 has disadvantages like low conversion rate, low selectivity of C_2, etc.[13, 14]. Dehydrogenation coupling is actually a nonoxidative conversion process as shown in Eq. (1), which includes the cleavage of C–H bond and the coupling of C–C

Received 4 December 2020; accepted 18 January 2021

① The work was supported by the National Key Research and Development Program of China (2017YFA0700102), Natural Science Foundation of China (91845202), Dalian National Laboratory for Clean Energy (DNL180404) and Strategic Priority Research Program of Chinese Academy of Sciences (XDB2000000)

② Corresponding author. Xie Kui, Professor. Tel: +86-591-63179173. E-mail: kxie@fjirsm.ac.cn

bond. A recent study showed that non-oxidative conversion can achieve a high methane conversion rate and ethylene selectivity of 48.1% and 48.4%, respectively[15].

$$2CH_4 = C_2H_4 + 4H^+ + 4e^- \quad (1)$$

Ceramic hydrogen permeable membranes can be used not only for separating hydrogen, but also for dehydrogenation coupling of methane to ethylene. The dense ceramic membrane[16, 17] has both proton and electron conductivity, which allows H_2 penetration with extremely high H_2 selectivity. Hydrogen adsorbs on the surface of the membrane and dissociates to form protons and electrons, as shown in Eq. (2). Then protons and electrons diffuse to the other side of the membrane under partial pressure of hydrogen, where they recombine to form hydrogen molecules (Eq. (3)). The phase diffusion process can be seen as protons jumping between the lattice oxygen and electrons being transferred into the body phase in the form of electron holes. Correspondingly, the use of ceramic hydrogen permeable membrane for DCM can *in situ* remove hydrogen from the reaction area (Eqs. (4) and (5)). It helps to break the thermodynamic equilibrium and the methane coupling equilibrium can be driven to move towards the C_2 product, thus increasing the conversion rate[18-20].

$$H_2 = 2H^+ + 2e^- \quad (2)$$

$$2H^+ + 2e^- = H_2 \quad (3)$$

$$2CH_4 = C_2H_6 + H_2 \quad (4)$$

$$2CH_4 = C_2H_4 + 2H_2 \quad (5)$$

The ceramic mixed protonic and electronic conducting (MPEC) membranes can effectively separate hydrogen, thereby promoting methane conversion. $BaCeO_{3-\delta}$-based high temperature proton conductors exhibit excellent conductivity[21-23]. Y doped $BaCeO_{3-\delta}$ has high proton conductivity and electron conductivity at the same time, and thereafter it is an ideal hydrogen permeable material[24, 25]. Here, we use perovskite $BaCe_{0.9}Y_{0.1}Co_xO_{3-\delta}$ ($x = 0 \sim 0.1$) hydrogen permeation membrane to realize methane to ethylene. We *in-situ* constructed the metal-oxide interface by doping the transition metal Co in the BCY lattice. Then Co nanoparticles with good distribution were obtained by controlling the content of transition metals and heat treatment in a reducing atmosphere. Finally, we studied the hydrogen permeability of Co doped BCY and the influence of metal-oxide interface on the dehydrogenation coupling of methane.

2 EXPERIMENTAL

2. 1 Synthesis of materials and membrane preparation

The $BaCe_{0.9}Y_{0.1}Co_xO_{3-\delta}$ (BCYC*x*) powders were obtained by liquid phase combustion method. The $BaCO_3$, $Ce(NO_3)_2{\cdot}6H_2O$, $Y(NO_3)_3{\cdot}6H_2O$, $Co(NO_3)_2{\cdot}6H_2O$ and glycine were added to dilute nitric acid solution (pH = 2.0). A clear and transparent solution will be obtained after heating and stirring. The BCYC*x* precursor was then heated to combustion and sintered at 1000 ℃ for 2 h in air[26]. The non-stoichiometric BCYC*x* (x = 0, 0.01, 0.05 and 0.1) are denoted as BCY, BCYC01, BCYC05, and BCYC10, respectively. The terpineol and ethocel ($[C_6+2nH_7+8nO_2+4n]_x$) were mixed at a mass ratio of 19:1. Then add the $BCYC_x$ powder to the mixture at a mass ratio of 1:1 to form $BCYC_x$ slurry for further use. The BCYC*x* powder and tapioca starch were mixed uniformly at the mass ratio of 7:3 and then pressed into tablets. Then these tablets were slowly heated up to 700 ℃ at a heating rate of 1 ℃·min^{-1}, which will make holes to form a porous scaffold. In order to achieve BCYC*x* dense layer, the BCYC*x* slurry was suspended-coated on the BCY porous support using a suspension coater with the suspension-coating rate of 6000 r·min^{-1}. After that the suspended-coated disks were sintered at 700 ℃ for 2 h and the same operation was repeated three times. Finally, the suspended membranes were calcined at 1450 ℃ for 10 h to achieve porous-dense hydrogen permeable membranes that were also called asymmetric membranes in our experiment[27].

2. 2 Material characterization

The phases of the BCYC*x* samples are characterized by X-ray diffraction (XRD) with Cu-*Kα* tube configuration (Miniflex600, Japan, $2\theta = 20°\sim80°$, 10°·min^{-1}). The element valence of the oxidized and reduced BCYC*x* samples are analyzed by X-ray photoelectron spectroscopy (XPS) equipped with Al-K*α* X-ray source (ESCALAB 250Xi, USA). The cross sectional microstructures of the membranes and metal nanoparticles are observed by Scanning electron microscope (SEM, SU-8010, Japan).

2. 3 Hydrogen permeability

The BCYC*x* membrane was sealed in an alumina tube with ceramic adhesive (JD-767, Jiudian, China), as shown in Fig. 1. Then, the membrane was heated by vertical furnace (OTF-1200X, Kejing, China) and the temperature was controlled from 950 to 1100 ℃. The diameter of each membrane was 15 mm, and the effective area was about 0.5 cm^2. A mixture of hydrogen and helium with a flow rate of 80 mL·min^{-1} is passed into the feed side of the membrane. Meanwhile, the pure argon with a flow rate of 30 mL·min^{-1} is

passed into the sweep side. All gases need to be calibrated with a mass flow controller (D08-3F, Sevenstar, China). The sweep gas will bring out the hydrogen permeated from the feed side, then enter into the online gas chromatograph (GC-2014, Shimazu, Japan) for quantitative analysis. The formula for calculating hydrogen permeation flux is as follows[28]:

$$J_{H_2}\,(mL/min\ cm^2) = (C_{H_2} - \frac{\sqrt{2}F_{H_2}C_{He}}{F_{He}}) \times \frac{F}{S} \qquad (6)$$

Where C_{H_2} , C_{He} are the hydrogen and helium concentrations from gas chromatograph analysis; F_{H_2} and F_{He} are the flow rates of hydrogen and helium on the feed side, respectively; F is the total flow rate of outlet gases on the sweep side; and S is the effective membrane area. Only when the leakage percentage of helium is less than 5%, can the formula reliably calculate the hydrogen permeability. In addition, the gas chromatograph has three consecutive sampling tests to further avoid the error of the experimental operation.

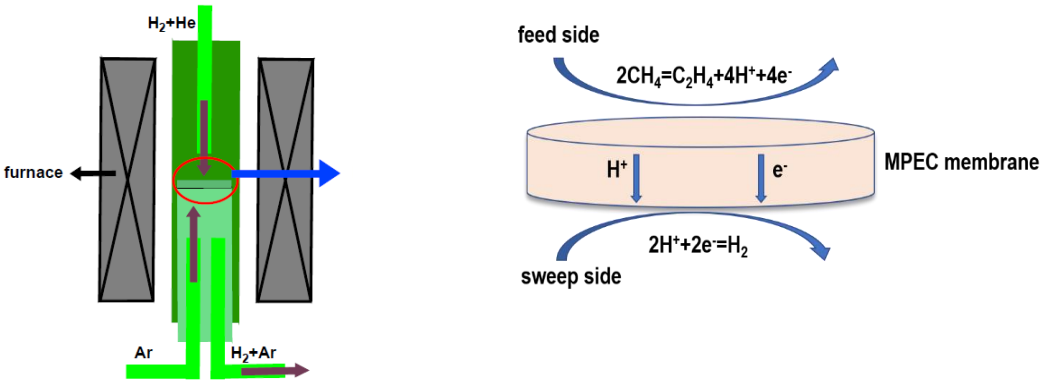

Fig. 1. Mechanism of methane dehydrogenation coupling with mixed protonic-electronic conducting (MPEC) membrane

3 RESULTS AND DISCUSSION

3. 1 Crystal structure

Fig. 2a is the XRD pattern of oxidized BCY powder doped Co in different stoichiometric ratios. We can observe that the phase of Co-doped BCY powder has no impurity peaks, which demonstrates that the Co element is completely doped into BCY lattice and keeps the perovskite phase unchanged. Fig. 2b is the XRD pattern of the powders reduced in pure hydrogen at 800 ℃ for 3 h. The XRD pattern shows that the Co doped BCY powders still maintain the perovskite structure after high temperature reduction. The peak of Co metal can be clearly observed, which means Co metal has been successfully restored to the surface BCY. The standard card that matches the Co metal after reduction at 800 ℃ is PDF (Powder Diffraction File) #05-0727.

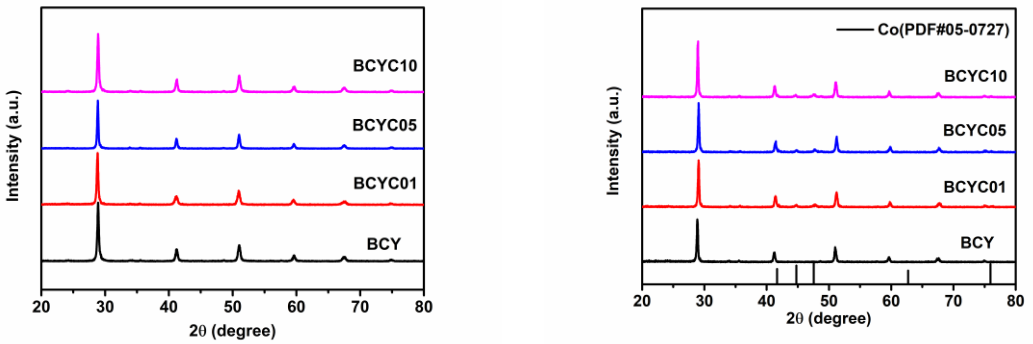

(a) **(b)**

Fig. 2. X-ray diffraction (XRD) patterns of BCYC*x* (*x* = 0, 0.01, 0.05, 0.1) powders. (a) Oxidized samples, (b) Reduced samples

3. 2 Elemental valence

Fig. 3 is the XPS diagram of BCYC05 powder in the oxidation and reduction states of Ce3*d* and Co2*p*. From Figs. 3a and 3c, we can see that the valence state of Ce element maintains constant after reduction in pure hydrogen. In Fig. 3b, the Co element of oxidized BCYC05 has two peaks, $Co^{2+}2p_{1/2}$ and $Co^{2+}2p_{3/2}$. However, as shown in Fig. 3d, the peaks of $Co^{0}2p_{3/2}$ and $Co^{0}2p_{1/2}$ are observed at 778.3 and 793.3 eV[29], showing the valence state of Co decreases from high- to low-valence state after being treated in a reducing atmosphere. It also proves that the Co metal has been successfully restored to the surface BCY. The above analysis results are quite consistent with those of XRD.

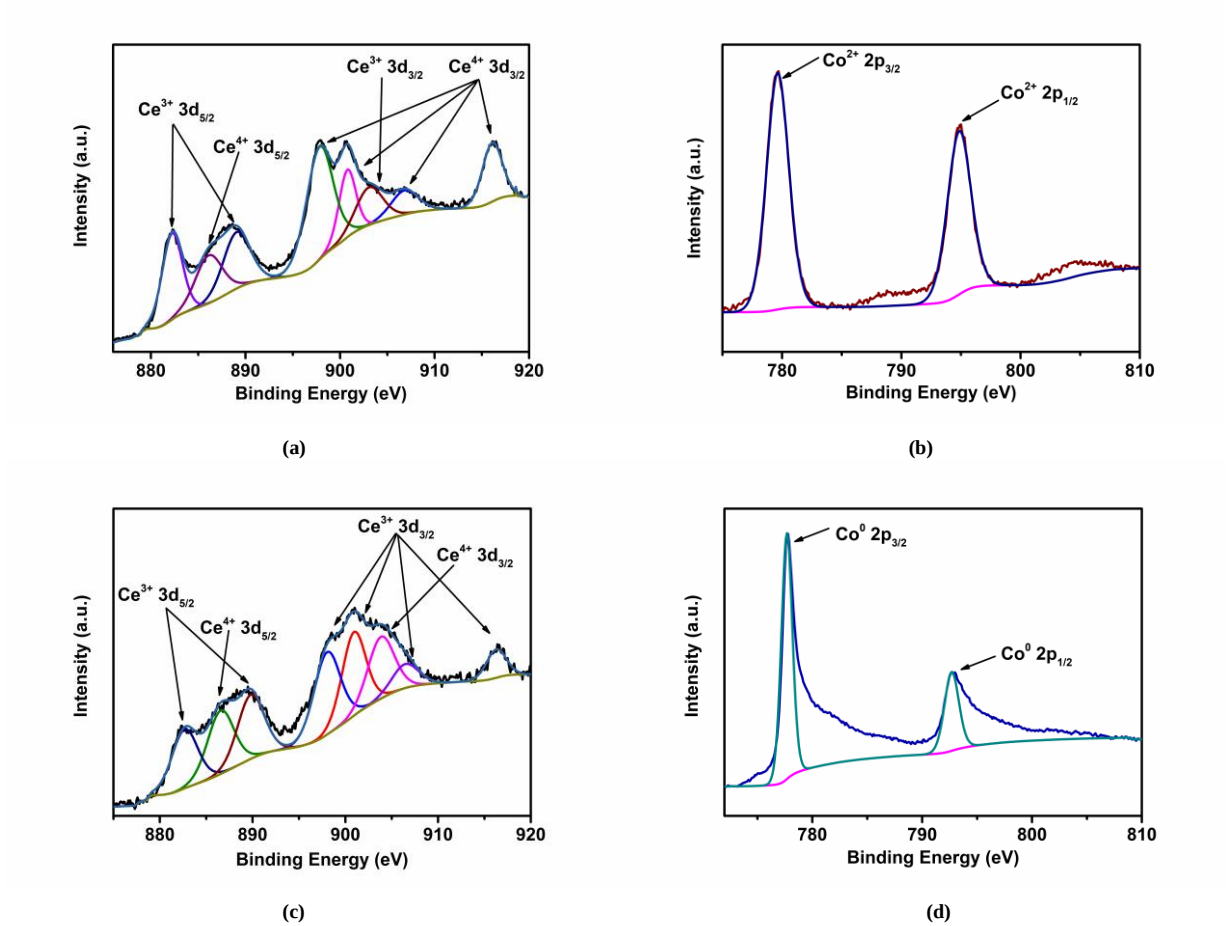

Fig. 3. XPS of oxidized BCYC05 sample: Ce3*d* (a) and Co2*p* (b); XPS of reduced BCYC05 sample: Ce3*d* (c) and Co2*p* (d)

3. 3 Microstructure

The cross-section microstructure of the BCYC05 membrane is performed in Fig. 4a. The entire BCYC05 membrane sintered at 1500 ℃ for 10 h has two physical structures, a 70 μm-thick dense layer and a porous substrate with a thickness of about 400 μm. In addition, the dense layer combines well with the porous support and the pore distribution is relatively uniform. Fig. 4b is the SEM images of porous substrates of BCYC05 after being reduced in hydrogen for 3 h at 850 ℃. We can see that cobalt nanoparticles with the median size of 75 nm are uniformly loaded on the BCY scaffold. Moreover, cobalt nanoparticles can be tightly bound to the BCY substrate to form metal-oxide interface, which provides lots of active sites for the conversion of CH_4 to C_2H_4.

3. 4 Hydrogen permeation of BCY, BCYC01, BCYC05 and BCYC10 membranes

To study the hydrogen permeability of different contents of Co doped BCY, hydrogen separation experiments are carried out from 950 to 1100 ℃. The hydrogen permeation of BCY, BCYC01, BCYC05 and BCYC10 membranes at different temperature is shown in Fig. 5a. The hydrogen permeation flux increases with the increase of temperature because the surface exchange reaction and the protonic bulk diffusion are accelerated at high temperature, which ultimately promotes the hydrogen permeation[30]. Additionally, we can find that the hydrogen permeability of BCYC05 membrane is better than other membranes in the same test interval. The

maximum hydrogen permeation flux, 0.205 mL·min^{-1}·cm^{-2}, is obtained at 1100 ℃. In order to explore the stability of the membrane at high temperature, long-term hydrogen permeation measurements of BCYC05 membrane are researched. As shown in Fig. 5b, the hydrogen permeability is kept relatively constant after 80 h operation at the test temperature. This result indicates that the BCYC*x* materials have long-term stability in hydrogen permeation.

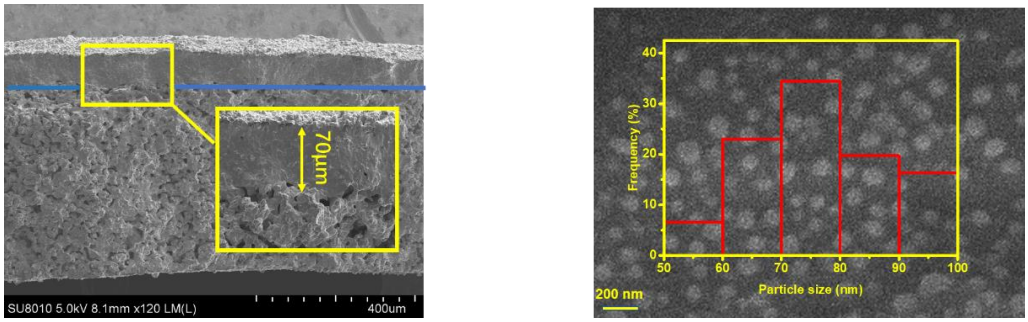

(a) **(b)**

Fig. 4. (a) The cross sectional microstructure of the asymmetric BCYC05 membrane. (b) SEM micrograph of the reduced BCYC05 sample

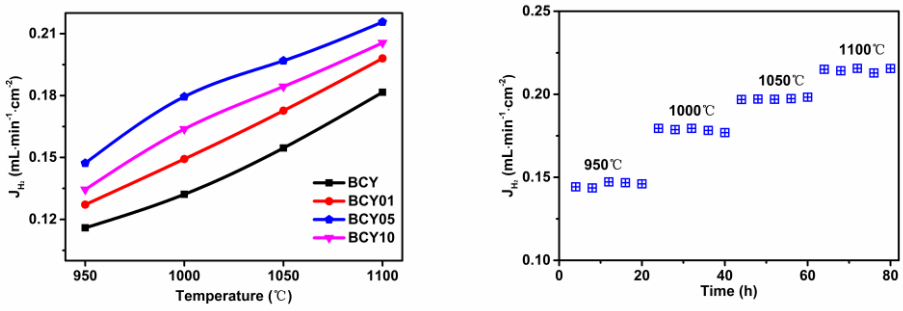

(a) **(b)**

Fig. 5. (a) Hydrogen permeation fluxes of the BCYC*x* (*x* = 0, 0.01, 0.05, 0.1) membranes, (b) Long-term hydrogen permeation through BCYC05 membrane at different temperature

3. 4 DCM performance

The porous-dense BCYC*x* (*x* = 0, 0.01, 0.05 and 0.1) membranes are used to test dehydrogenation coupling of methane reaction. Fig. 6a shows the product analysis results of all samples with different stoichiometric ratios for DCM from 950 to 1100 ℃. Obviously, with the temperature increasing, the concentrations of C_2 (C_2H_4 + C_2H_6) and H_2 have an increasing tendency. We can observe that the highest concentrations C_2 reaches 5.66% (5.25% C_2H_4 + 0.41% C_2H_6) at 1100 ℃. Fig. 6b shows the methane conversion of all samples from 950 to 1100 ℃, from which we can see that sample BCYC05 has the optimal catalytic activity. The highest conversion of methane gets to 24.8%. According to Fig. 6c, sample BCYC05 also has the highest C_2 selectivity, which further indicates that the metal-oxide interface contributes not only to the C–H bond activation but also to the reduction of carbon deposition. Fig. 6d depicts that the highest C_2 yield is up to about 11.3% at 1100 ℃ with BCYC05. In addition, the hydrogen is transported from the feed side to the sweep side through the hydrogen permeable membrane, which helps to break the traditional thermodynamic equilibrium and thus enhances the catalytic conversion of methane. On the other hand, the long-term stability of methane conversion and C_2 selectivity are researched at 1100 ℃ with sample BCYC05, as shown in Figs. 6e and 6f, respectively. It can be seen that perovskite-type BCYC*x* materials are relatively stable in the DCM reaction.

4 CONCLUSION

In this work, perovskite-type porous-dense BCYC*x* hydrogen permeation membranes are successfully prepared by suspension coating process. We studied the hydrogen permeation flux and the stability of BCYC*x* at different temperature. The BCYC05 has the highest hydrogen permeation and it can run almost stably for more than 80 h from 950 to 1100 ℃. Moreover, we studied the DCM

performance of BCYC*x* (*x* = 0, 0.01, 0.05 and 0.1). After being reduced, Co nanoparticles appeared on the surface of BCY porous scaffold to form metal-oxide interface, which will promote methane conversion and enhance carbon deposition resistance. The methane conversion and C_2 selectivity reach 24.8% and 45.6%, respectively. Additionally, no obvious decay is observed after 30 h operation.

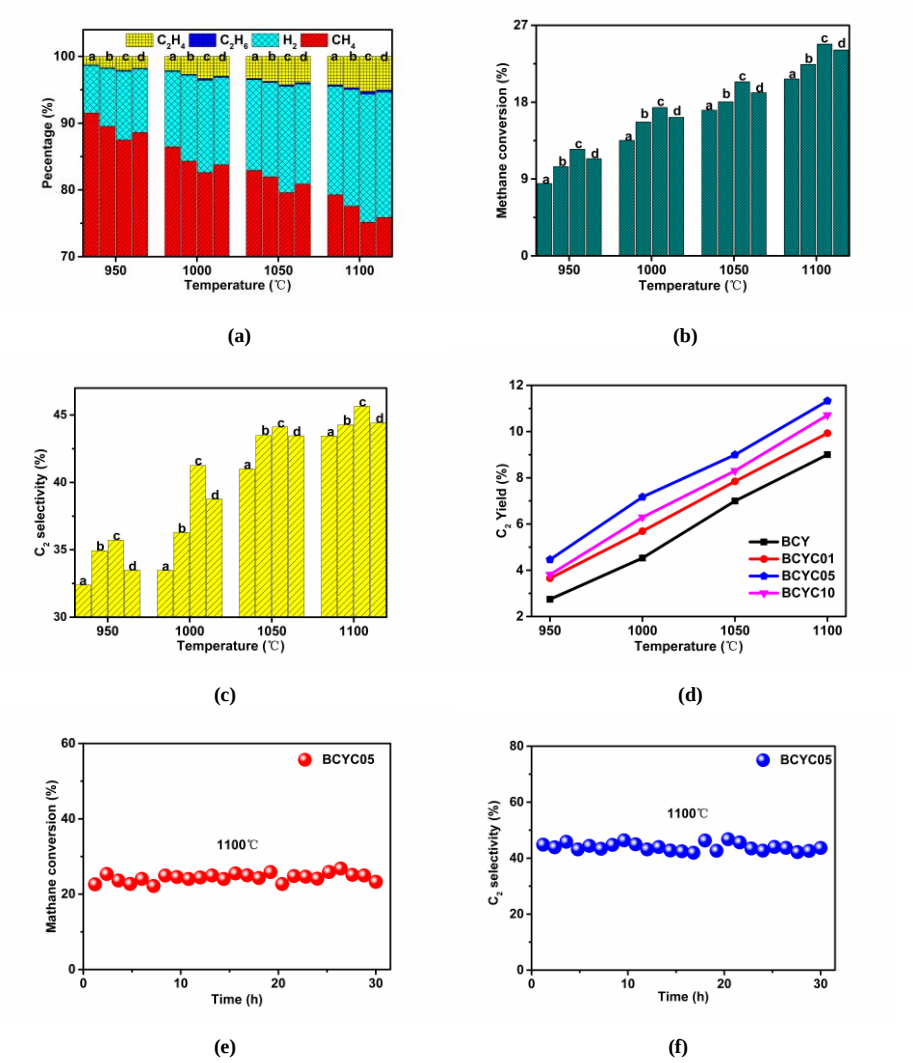

a: BCY, b: BCYC01, c: BCYC05, d: BCYC10

Fig. 6. Performance of DCM reaction with different membranes. (a) The product analysis, (b) Methane conversion, (c) C_2 product selectivity and (d) C_2 product yield. The stability test of (e) methane conversion and (f) C_2 product selectivity at 1100 ℃ with the BCYC05 membrane

REFERENCES

(1) Ren, T.; Patel, M.; Blok, K. Olefins from conventional and heavy feedstocks: energy use in steam cracking and alternative processes. *Energy* **2006**, 31, 425–451.

(2) Lee, M. H.; Nagaraja, B. M.; Lee, K. Y.; Jung, K. D. Dehydrogenation of alkane to light olefin over PtSn/θ-Al_2O_3 catalyst: effects of Sn loading. *Catal. Today* **2014**, 232, 53–62.

(3) Sattler, J. J.; Ruiz-Martinez, J.; Santillan-Jimenez, E.; Weckhuysen, B. M. Dehydrogenation of light alkanes on metals and metal oxides. *Chem. Rev.* **2014**, 114, 10613–10653.

(4) Lange, J. P. Methanol synthesis: a short review of technology improvements. *Catal. Today* **2001**, 64, 3–8.

(5) Xu, S. T.; Zheng, A. M.; Wei, Y. X.; Chen, J. R.; Li, J. Z.; Chu, Y. Y.; Zhang, M. Z.; Wang, Q. Y.; Zhou, Y.; Wang, J. B.; Deng, F.; Liu, Z. M. Direct observation of cyclic carbenium ions and their role in the catalytic cycle of the methanol-to-olefin reaction over chabazite zeolites. *Angew. Chem. Int. Ed.* **2013**, 52, 11564–11568.

(6) Tian, P.; Wei, Y. X.; Ye, M.; Liu, Z. M. Methanol to olefins (MTO): from fundamentals to commercialization. *ACS Catal.* **2015**, 5, 1922–1938.

(7) Li, L. P.; Chen, Y. Y.; Xu, S. T.; Li, J. F.; Dong, M.; Liu, Z. W.; Jiao, H. J.; Wang, J. G.; Fan, W. B. Oriented control of Al locations in the framework of Al–Ge–ITQ-13 for catalyzing methanol conversion to propene. *J. Catal.* **2016**, 344, 242–251.

(8) Zhao, X. B.; Wang, L. Y.; Li, J. Z.; Xu, S. T.; Zhang, W. N.; Wei, Y. X.; Guo, X. W.; Tian, P.; Liu, Z. M. Investigation of methanol conversion over high-Si beta zeolites and the reaction mechanism of their high propene selectivity. *Catal. Sci. Tech.* **2017**, 7, 5882–5892.

(9) Cheng, K.; Gu, B.; Liu, X. L.; Kang, J. C.; Zhang, Q. H.; Wang, Y. Direct and highly selective conversion of synthesis gas into lower olefins: design of a bifunctional catalyst combining methanol synthesis and carbon-carbon coupling. *Angew. Chem. Int. Ed.* **2016**, 55, 4725–4728.

(10) Cheng, K.; Ordomsky, V. V.; Virginie, M.; Legras, B.; Chernavskii, P. A.; Kazak, V. O.; Cordier, C.; Paul, S.; Wang, Y.; Khodakov, A. Y. Support effects in high temperature Fischer-Tropsch synthesis on iron catalysts. *Appl. Catal. A: Gen.* **2014**, 488, 66–77.

(11) Zhu, C. L.; Hou, S. S.; Hu, X. L.; Lu, J. H.; Chen, F. L.; Xie, K. Electrochemical conversion of methane to ethylene in a solid oxide electrolyzer. *Nat. Commun.* **2019**, 10, 1173–8.

(12) Bajec, D.; Kostyniuk, A.; Pohar, A.; Likozar, B. Department of nonoxidative methane activation, coupling, and conversion to ethane, ethylene, and hydrogen over Fe/HZSM-5, Mo/HZSM-5, and Fe-Mo/HZSM-5 catalysts in packed bed reactor. *Int. J. Energy Res.* **2019**, 43, 6852–6868.

(13) Schwach, P.; Hamilyon, N.; Eichelbaum, M.; Thum, L.; Lunkenbein, T.; Schlögl, R.; Trunschke, A. Structure sensitivity of the oxidative activation of methane over MgO model catalysts: II. Nature of active sites and reaction mechanism. *J. Catal.* **2015**, 329, 574–587.

(14) Noon, D.; Seubsai, A.; Senkan, S. Oxidative coupling of methane by nanofiber catalysts. *ChemCatChem.* **2013**, 5, 146–149.

(15) Guo, X. G.; Fang, G. Z.; Li, G.; Ma, H.; Fan, H. J.; Yu, L.; Ma, C.; Wu, X.; Deng, D. H.; Wei, M. M.; Tan, D. L.; Si, R.; Zhang, S.; Li, J. Q.; Sun, L. T.; Tang, Z. C.; Pan, X. L.; Bao, X. H. Direct, nonoxidative conversion of methane to ethylene, aromatics, and hydrogen. *Science* **2014**, 344, 616–619.

(16) Norby, T. Solid-state protonic conductors: principles, properties, progress and prospects. *Solid State Ionics* **1999**, 125, 1–11.

(17) Katahira, K.; Kohchi, Y.; Shimura, T.; Iwahara, H. Protonic conduction in Zr-substituted $BaCeO_3$. *Solid State Ionics* **2000**, 138, 91–98.

(18) Chiang, P. H.; Eng, D.; Stoukides, M. Electrocatalytic nonoxidative dimerization of methane over Ag electrodes. *Solid State Ionics* **1993**, 61, 99–103.

(19) Chiang, P. H.; Eng, D.; Tsiakaras, P.; Stoukides, M. Ion transport and polarization studies in a proton conducting solid electrolyte cell. *Solid State Ionics* **1995**, 77, 305–310.

(20) Sakbodin, M.; Wu, Y. Q.; Oh, S. C.; Wachsman, E. D.; Liu, D. X. Hydrogen-permeable tubular membrane reactor: promoting conversion and product selectivity for non-oxidative activation of methane over an Fe©SiO_2 catalyst. *Angew. Chem. Int. Ed.* **2016**, 55, 16149–16152.

(21) Danilov, N.; Lyagaeva, J.; Kasyanova, A.; Vdovin, G.; Medvedev, D.; Demin, A.; Tsiakaras, P. The effect of oxygen and water vapor partial pressures on the total conductivity of $BaCe_{0.7}Zr_{0.1}Y_{0.2}O_{3-\delta}$. *Ionics* **2017**, 23, 795–801.

(22) Islam, Q. A.; Raja, M. W.; Basu, R. N. Zr- and Tb-doped barium cerate-based cermet membrane for hydrogen separation application. *J. Am. Ceram. Soc.* **2017**, 100, 1360–1367.

(23) Lin, Y. S. Microporous and dense inorganic membranes: current status and prospective. *Sep. Purif. Technol.* **2001**, 25, 39–55.

(24) Guan, J.; Dorris, S. E.; Balanehandran, U.; Liu, M. Transport properties of $BaCe_{0.95}Y_{0.05}O_{3-\alpha}$ mixed conductors for hydrogen separation. *Solid State Ionics* **1997**, 100, 45–52.

(25) Ma, G. L.; Shimura, T.; Iwahara, H. Ionic conduction and nonstoichiometry in $BaCe_{0.9}Y_{0.1}O_{3-\alpha}$. *Solid State Ionics* **1998**, 110, 103–110.

(26) Zhang, X. R.; Ye, L. T.; Li, H.; Chen, F. L.; Xie, K. Electrochemical dehydrogenation of ethane to ethylene in a solid oxide electrolyzer. *ACS Catal.* **2020**, 10, 3505–3513.

(27) Chen, L.; Liu, L. F.; Xue, J.; Zhuang, L. B.; Wang, H. H. Asymmetric membrane structure: an efficient approach to enhance hydrogen separation performance. *Sep. Purif. Technol.* **2018**, 207, 363–369.

(28) Chen, Y.; Wei, Y. Y.; Zhuang, L. B.; Xie, H. Q.; Wang, H. H. Effect of Pt layer on the hydrogen permeation property of $La_{5.5}W_{0.45}Nb_{0.15}Mo_{0.4}O_{11.25-\delta}$ membrane. *J. Membr. Sci.* **2018**, 552, 61–67.

(29) Majumdar, D.; Spahn, R. G.; Gau, J. S. X-ray photoelectron spectroscopy studies on the oxidation behavior of CoNi thin films. *J. Electrochem. Soc.* **1987**, 134, 1825–1829.

(30) Zhang, Q. Y.; Han, J. J.; Huang, Y.; Chen, Y.; Yan, X.; Lang, W. Z. Effect of Ba non-stoichiometry in $Ba_{1-x}Zr_{0.1}Ce_{0.7}Y_{0.2}O_{3-\delta}$ on its structure defect, sinterability and hydrogen permeability. *Ceram. Int.* **2020**, 46, 19564–19573.